Narrowband terahertz radiation by impulsive stimulated Raman scattering in an above-room-temperature organic ferroelectric benzimidazole

M. Sotome,[1] N. Kida,[1,*] S. Horiuchi,[2] and H. Okamoto[1,3]

[1]*Department of Advanced Materials Science, The University of Tokyo, 5-1-5 Kashiwa-no-ha, Chiba 277-8561, Japan*

[2]*National Institute of Advanced Industrial Science and Technology (AIST), Tsukuba 305-8562, Japan*

[3]*AIST-UTokyo Advanced Operando-Measurement Technology Open Innovation Laboratory, National Institute of Advanced Industrial Science and Technology, Chiba 277-8568, Japan*

(Received 27 March 2018; revised manuscript received 13 June 2018; published 26 July 2018)

In noncentrosymmetric media, optical rectification is known to be a general mechanism of the generation of terahertz electromagnetic waves. Here, we show that effective terahertz radiation is possible via a different mechanism in a hydrogen-bonded organic molecular ferroelectric 5,6-dichloro-2-methylbenzimidazole (DCMBI). By the irradiation of a femtosecond laser pulse on a single crystal of DCMBI at room temperature, we observe a strong terahertz radiation. The emitted terahertz wave consists of three oscillatory components, the frequencies of which agree with those of Raman- and infrared-active phonon modes. This suggests that the terahertz radiation is attributed to polarization modulations by infrared-active phonons excited via impulsive stimulated Raman scattering processes. By taking into account the Raman polarizability tensor and dipole moment for each phonon, we succeeded in reproducing not only the spectrum of the terahertz radiation, but also its time characteristic. The analysis method is discussed in detail. Our result provides an alternative method for the light-induced terahertz radiation in organic ferroelectrics.

DOI: 10.1103/PhysRevA.98.013843

I. INTRODUCTION

The second-order optical nonlinearity in noncentrosymmetric media is useful for the frequency conversion of light, which includes not only the sum and difference frequency generation but also the optical parametric effect [1,2]. In this context, ferroelectric materials are being intensively studied [1]. In oxide ferroelectrics such as $LiNbO_3$ and KH_2PO_4, highly efficient second-order optical nonlinearity has been reported, which is enough for practical use as nonlinear optical materials. Explorations of organic ferroelectrics are also important, since organic materials have advantages due to their low cost and environmentally benign characteristics. However, it had been reported that their Curie temperatures are much lower than room temperature. Recently, above-room-temperature ferroelectricity has been found in hydrogen-bonded molecular crystals having π-electron systems [3] such as 4,5-dihydroxy-4-cyclopentence-1,2,3-trione (croconic acid) [4] and 2-phenylmalondialdehyde [5]. In these materials, cooperative proton displacements and asymmetric π-electron configurations along the hydrogen-bonded direction cause the ferroelectric polarization.

In croconic acid and 2-phenylmalondialdehyde, we have recently demonstrated that a terahertz electromagnetic wave can be radiated by an irradiation of a femtosecond laser pulse [6,7] and that the terahertz radiation can be ascribed to a difference frequency generation (DFG) within an incident laser pulse, which is described by the second-order nonlinear optical susceptibility $\chi^{(2)}$. This process is sometimes called optical rectification (OR) [8] and is recognized as a typical terahertz-radiation mechanism in various noncentrosymmetric media such as ZnTe [9] and 4-*N*,*N*-dimethylamino-4′-*N*′-methyl stilbazolium tosylate (DAST) [10].

In the present study, we report that effective terahertz radiation is possible via a different mechanism in a hydrogen-bonded organic molecular ferroelectric, 5,6-dichloro-2-methylbenzimidazole (DCMBI) [11]. By the irradiation of a femtosecond laser pulse on a single crystal of DCMBI, we observe an emission of a terahertz wave consisting of several oscillatory components, which cannot be attributed to the OR mechanism. The central frequencies of those oscillations correspond to three phonon modes, which are both Raman and infrared active, indicating that the terahertz radiation originates from the infrared-active phonons excited via impulsive stimulated Raman scattering processes. By taking into account the polarizabilities of Raman scatterings and the dipole moments of infrared absorptions of phonons, we show that both the spectrum and time characteristic of the terahertz radiation are well simulated.

The crystal system of DCMBI is orthorhombic with a space group of $Pca2_1$ (point group of $mm2$), as illustrated in Fig. 1(a) [11]. The imidazole molecules with a large dipole moment are connected by intermolecular hydrogen bonds along the c axis, as indicated by thick red (gray) lines. The protons are placed at off-center positions with asymmetric π-electron distribution, resulting in a large spontaneous polarization P ($\sim 10\,\mu C/cm^2$) along the hydrogen-nitrogen-bond direction, i.e., the c axis [11]. The polarization reversal is possible by cooperative proton transfers and π-bond switching.

*kida@k.u-tokyo.ac.jp

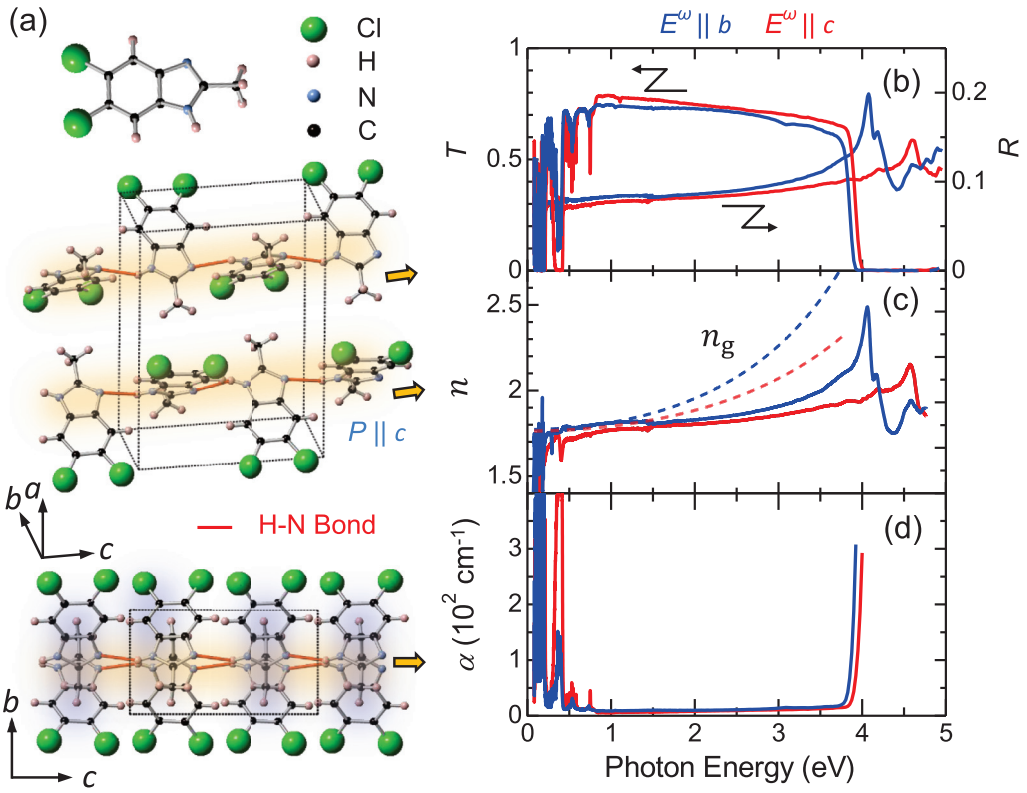

FIG. 1. (a) Schematics of molecular and crystal structures of 5,6-dichloro-2-methylbenzimidazole. Spontaneous polarization P (arrows) appears along the H-N bond direction (c axis) indicated by the thick red (gray) line. The imidazole molecules are indicated by the shaded blue (gray) area, which is perpendicular to the direction of P (arrow). (b) Polarized transmittance T and reflectivity R, (c) refractive index n, and (d) absorption coefficient α spectra for $E^{\omega}||b$ [blue (gray) lines] and $E^{\omega}||c$ [red (light gray) lines]. The group refractive index n_g spectra are also shown by dotted lines in (c).

II. EXPERIMENTAL PROCEDURES

Single crystals of DCMBI were grown by a previously reported method [11]. For the steady-state reflectivity and transmission measurements in the visible to midinfrared region, we used a Fourier-transformed infrared spectrometer (FTIR) and a grating spectrometer, both of which are equipped with specially designed optical microscopes. For the transmission measurement in the terahertz region, we adopted a terahertz time-domain spectroscopy (TDS) [9], in which a mode-locked Ti:sapphire laser with the central wavelength of 800 nm (1.55 eV), the repetition rate of 80 MHz, and the pulse width of 100 fs was used as a light source. A (110)-oriented ZnTe emitter excited by a Ti:sapphire laser pulse was used as a light source and a photoconductive antenna with low-temperature-grown GaAs excited by a part of the Ti:sapphire laser pulse was used as a detector. We used a Raman spectrometer equipped with a He-Ne laser (632.8 nm) as the light source and an optical microscope. In the terahertz-radiation experiments, the mode-locked Ti:sapphire laser mentioned above was used as an excitation source and the electric-field waveform of the terahertz radiation was also detected by an antenna. The spot diameter was ~25 μm. In order to exclude the water absorption, we performed the experiments in the dried air. All the optical measurements were carried out at 294 K.

III. RESULTS

A. Polarized optical spectra from the visible to midinfrared region

First, we show the fundamental optical properties from the visible to midinfrared region. Figure 1(b) shows the polarized reflectivity R and transmittance T spectra, which are measured on a single crystal with the thickness d of 150 μm for the electric fields of light E^{ω} parallel to the b axis ($E^{\omega}||b$) and to the c axis ($E^{\omega}||c$). A sharp decrease of T above 3.8 eV for $E^{\omega}||b$ is attributable to the π-π^* transition peaked at 4.1 eV, which is clearly observed in the R spectrum along the b axis. T also decreases at almost the same position for $E^{\omega}||c$, suggesting that the π-π^* transition has a finite component along the c axis. Spiky structures below 0.5 eV are due to optical phonons. We calculated the spectra of the refractive index n from R spectra by the Kramers-Kronig transformation and the spectra of the absorption coefficient α from the R and T spectra using the relationship $\alpha = -\frac{1}{d}\ln[\frac{T}{(1-R)^2}]$. The obtained n and α spectra are shown in Figs. 1(c) and 1(d), respectively. From 1 to 3 eV, no optical anisotropy is observed and n is nearly constant (~1.8) and α is negligibly small (<6 cm^{-1}). We reproduce n spectra by using the Sellmeier relation and estimate the group refractive index n_g spectra, which are shown by dotted lines in Fig. 1(c). n_g at 1.55 eV for $E^{\omega}||b$ and $E^{\omega}||c$ are 1.88 and 1.83, respectively.

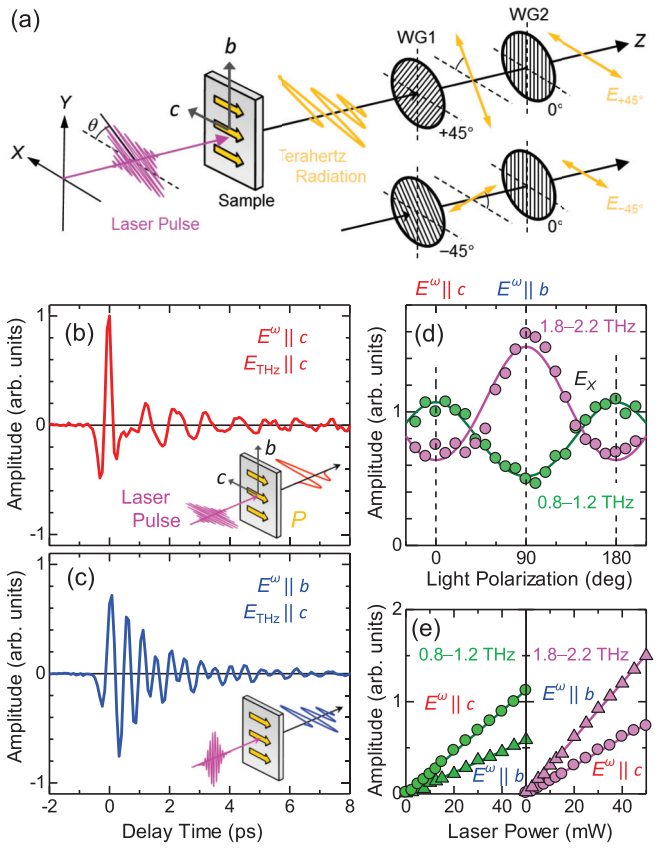

FIG. 2. (a) Schematic for vector analysis using two wire-grid polarizers. X-axis component of terahertz waveforms for (b) $E^{\omega}||c$ and (c) $E^{\omega}||b$. (d) Light-polarization angle θ and (e) laser power dependences of the terahertz electric fields in the frequency range of 0.8–1.2 THz and 1.8–2.2 THz.

B. Terahertz radiation

In organic ferroelectrics, domains with different polarization directions sometimes coexist in an as-grown single crystal [6,12]. To investigate a domain structure, we measured the maximum value of the terahertz electric field at 0 ps at various positions of the DCMBI crystal using a raster scan and obtained the domain image over the crystal [6,12–15]. The result of DCMBI revealed that the crystal consists of a single-domain state, which is detailed in the Supplemental Material, S1 [16]. In the terahertz-radiation experiment, a femtosecond laser pulse with a spot diameter of ∼25 μm is irradiated within a single-domain state.

The experimental setup in the laboratory coordinates XYZ is shown in Fig. 2(a). The experiment was performed on the same single crystal as used in the optical spectroscopy mentioned above. The LT-GaAs detector is set so that the X-axis component of the electric field $E_X(t)$ is selectively detected. Figures 2(b) and 2(c) show the time characteristics of $E_X(t)$ for the electric fields E^{ω} of the incident laser pulse parallel to the c and b axes ($E^{\omega}||c$ and $E^{\omega}||b$), respectively. The time origin is arbitrary. The laser power is fixed to 50 mW. For $E^{\omega}||c$, we can see a nearly single-cycle electric field around 0 ps, which is followed by an oscillatory component at least up to 8 ps. In contrast, for $E^{\omega}||b$, we observe a prominent oscillation signal, which seems to consist of several oscillatory components with different frequencies.

Next, we discuss the second-order nonlinear optical process related to the terahertz radiation, which is detailed in Appendix A. When the second-order nonlinear optical process is dominant, $E_X(\omega)$ is expressed as

$$E_X(\omega) \propto (d_{32}\sin^2\theta + d_{33}\cos^2\theta)I, \quad (1)$$

where I is the laser intensity and θ is the light-polarization angle relative to the X axis [Fig. 2(a)]. Figure 2(d) shows θ dependence of $E_X(\omega)$ integrating in the frequency range of 0.8–1.2 THz and 1.8–2.2 THz, which are indicated by green (gray) and pink (light gray) circles, respectively. Equation (1) well reproduces θ dependence of $E_X(\omega)$ as shown by the solid lines; the ratios (d_{32}/d_{33}) are evaluated to be 0.54 and 1.54 by integrating in the frequency range of 0.8–1.2 THz and 1.8–2.2 THz, respectively. As shown in Fig. 2(e), the terahertz-radiation intensities are proportional to I as expected from Eq. (1). These results demonstrate that the second-order nonlinear optical effect dominates the light-induced terahertz radiation from crystalline DCMBI.

In the terahertz-radiation experiments, it is important to consider the phase-matching condition between an incident laser pulse and a generated terahertz wave. We calculate the coherence length $l_c(=\frac{\lambda}{2}\frac{1}{|n_g-n_{THz}|})$ along the b and c axes, where λ and n_{THz} are the wavelength and n of the emitted terahertz waves, respectively. From the polarized T measurements of a 397-μm-thick a-axis-oriented crystal by terahertz TDS, we estimated n_{THz} spectra, which is detailed in Appendix B. Using the values of $n_g = 1.83(1.88)$ at 1.55 eV [Fig. 1(c)] and $n_{THz} = 1.68-1.86\,(1.68–1.87)$ at 0.5–3 THz for $E^{\omega}||c$ ($E^{\omega}||b$), we obtain the spectrum of l_c; $l_c = 2.96$ mm at 1 THz (1.34 mm) for $E^{\omega}||c$ ($E^{\omega}||b$) (see Fig. 5 in Appendix B). As shown in Fig. 5(c), l_c shows the sharp increase, which originates from a good phase-matching condition ($n_g \sim n_{THz}$) due to the presence of the sharp dispersion of the phonon modes [17]. However, in both configurations, l_c at 0.5–3 THz is much longer than the sample thickness (150 μm), indicating the good phase-matching condition in terahertz-radiation experiments. This also excludes the generation of the narrowband terahertz radiation in DCMBI due to the resonant enhancement of l_c. In addition, the penetration depths ($1/\alpha = 1.6$ mm for $E^{\omega}||c$ and 1.0 mm for $E^{\omega}||b$) [Fig. 1(d)] of the incident laser pulse also far exceed the sample thickness (150 μm), so that terahertz waves are considered to be emitted from all of the DCMBI crystal. In the same experimental condition, we measured the terahertz radiation in a typical terahertz emitter of (110)-oriented ZnTe. The terahertz-radiation efficiency is comparatively high for both $E^{\omega}||c$ and $E^{\omega}||b$ and is estimated to be ∼24% and 17% of that in ZnTe.

To investigate the nature of the observed terahertz radiations, we performed the fast Fourier transformation of the obtained $E_X(t)$ profiles, which are shown by circles in Fig. 3(a). The frequency resolution (0.05 THz) is indicated by a pair of vertical lines. For $E^{\omega}||b$, three peak structures are clearly observed at 0.97, 1.8, and 1.98 THz, while for $E^{\omega}||c$, a peak at 0.97 THz is prominent. In addition, a broad structure seems to exist at 1.2–1.7 THz for both polarizations in common. The thick red (gray) line in Fig. 3(a) shows the

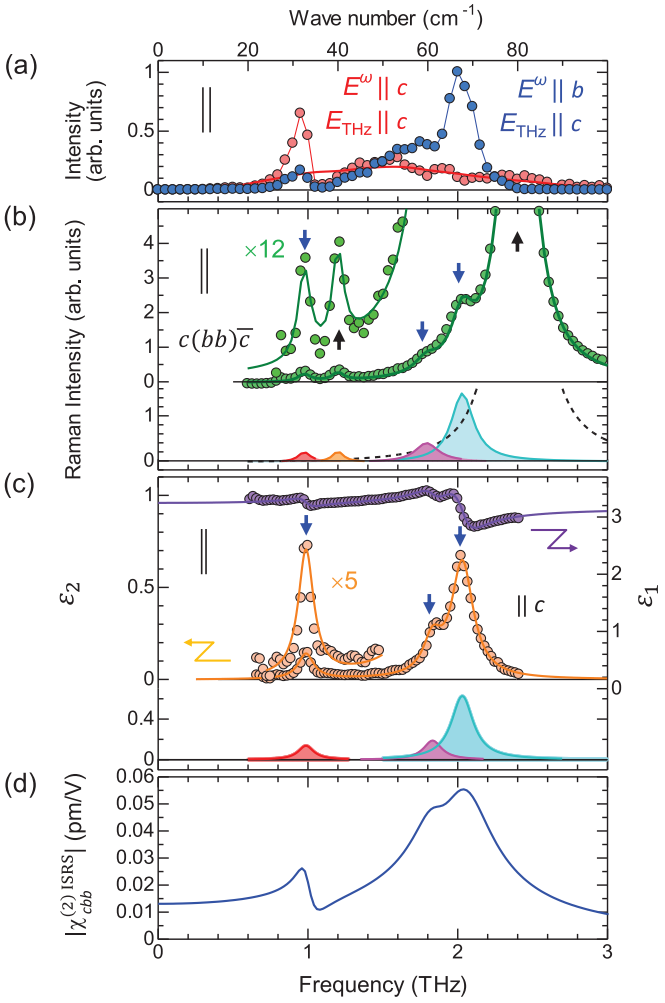

FIG. 3. (a) Intensity spectra of terahertz radiation for $E^{\omega}||c$ and $E^{\omega}||b$. (b) Raman scattering spectrum in $c(bb)\,\bar{c}$ configuration, which can be reproduced by assuming five Raman modes (shaded area and dotted line). (c) Real ε_1 and imaginary ε_2 parts of the dielectric constant spectrum along the c axis, which can be reproduced by three Lorentz oscillators (shaded area). (d) Evaluated spectrum of the second-order nonlinear susceptibility $|\chi^{(2)\mathrm{ISRS}}|$ due to the impulsive stimulated Raman scattering.

FFT spectrum obtained in the time-domain data from -2 to 1 ps for $E^{\omega}||c$, which is characterized by the single-cycle component around 0 ps. It is reasonable to consider that such a single-cycle component originates from the OR, which is a general mechanism of terahertz radiation in noncentrosymmetric media. On the other hand, a possible origin of the oscillatory structures [Figs. 2(b) and 2(c)] with the narrowband terahertz radiations [Fig. 3(a)] is the impulsive stimulated Raman scattering process, as discussed later. The DCMBI crystal has no space inversion symmetry, so that a Raman-active mode can be infrared active and then contribute to the terahertz radiation. To demonstrate this mechanism, we performed Raman and IR spectroscopies.

C. Polarized Raman and optical spectra in the terahertz region

We measured the polarized Raman spectra using *ab*-, *bc*-, and *ac*-surface crystals in the terahertz region, as detailed in Appendix C. According to the Raman selection rule with *mm*2 symmetry, $A_1(z)$ longitudinal-optical (LO) phonon modes become active in $c(bb)\bar{c}$ configuration; the Raman spectrum obtained in $c(bb)\bar{c}$ configuration is shown in Fig. 3(b) (circles), in which the five LO modes are identified at 0.99, 1.21, 1.80, 2.03, and 2.40 THz as shown by the vertical arrows. A Raman scattering intensity spectrum of each mode ($i = 1-5$) is given by the following formula [18].

$$I(\omega) = \frac{1}{1-\exp\left(-\frac{\hbar}{k_B T}\right)}\left[1-\left(\frac{n-1}{n+1}\right)^2\right]^2 \frac{2\hbar\omega_s^4 N^2}{\rho c^4 \omega_v} \times \sum_i^m \frac{a_i^2 \gamma_i \omega}{\left(\omega_i^2-\omega^2\right)+\gamma_i^2\omega^2}. \quad (2)$$

Here, n is a refractive index (1.7) at 633 nm [Fig. 1(c)], ρ the density (1.586 kg/m^3) [11], N the volume in a primitive cell (4.75×10^{27} m^{-3}), ω_s the center frequency of the scattering light, and c the velocity of light. ω_i, a_i, and γ_i are the central frequency, Raman polarizability tensor, and damping of the Raman modes, respectively. In Eq. (2), the first term shows the correction with the Bose-Einstein factor; the second term shows the correction for the reflection losses of the excitation light (633 nm) and the scattered light (~633 nm) at the sample surface. The third term dominates the Raman scattering intensity. Using Eq. (2), the Raman spectrum is almost reproduced as shown by the solid line in Fig. 3(b). Spectra of each mode are also shown by the dotted line and color (gray) lines in the lower part of Fig. 3(b). In order to evaluate the absolute value of a_i, we measured the Raman spectrum around 1330 cm^{-1} of a *c*-axis-oriented diamond for the $c(ab)\bar{c}$ configuration and compared its integrated intensity with that of each Raman band in DCMBI. The γ_i and a_i values thus obtained are listed in Table I.

Figure 3(c) shows the spectra of the real (ε_1) and imaginary (ε_2) part of the dielectric constant for $E^{\omega}||c$ obtained from the terahertz TDS on a *bc* plane in a 397-μm-thick single crystal. We can see sharp peak structures at 0.99, 1.83, and 2.03 THz indicated by vertical arrows in the ε_2 spectrum and the corresponding dispersions in the ε_1 spectrum. Three peak structures at 0.99, 1.83, and 2.03 THz in Fig. 3(c) are also observed in the Raman spectrum in Fig. 3(b), while no IR-active modes corresponding to the Raman peaks at 1.21 and 2.40 THz (indicated by black upward arrows) are observed. In order to estimate the dipole moment μ_i of each IR-active mode ($i = 1-3$), we performed the fitting analysis using three Lorentz oscillators, which are given by

$$\epsilon_1(\omega) = \epsilon_\infty + \sum_{i=1}^{3}\left[\frac{f_i\omega_i^2\left(\omega_i^2-\omega^2\right)}{\left(\omega_i^2-\omega^2\right)^2+\gamma_i^2\omega^2}\right], \quad (3)$$

$$\epsilon_2(\omega) = \sum_{i=1}^{3}\left[\frac{f_i\omega_i^2\gamma_i\omega}{\left(\omega_i^2-\omega^2\right)^2+\gamma_i^2\omega^2}\right], \quad (4)$$

where f_i is represented by $f_i = \frac{2Ne^2}{\epsilon_0\hbar\omega_i}\mu_i$. The obtained μ_i are listed in Table I. The calculated ε_1 and ε_2 spectra well reproduce the experimental ones as shown by the solid lines in Fig. 3(c). In this analysis, the high-frequency dielectric constant is set to be 3.16. Each ε_2 component was also shown in the lower

TABLE I. Obtained fitting parameters of Raman-active and infrared-active phonon modes and comparison with terahertz radiation polarized along the c axis for $E^{\omega}||b$.

Terahertz radiation	Raman			Infrared		
$E^{\omega}||b$, $E_{\mathrm{THz}}||c$	$c(bb)\bar{c}$			$\|\|c$		
$\omega/2\pi$ (THz)	$\omega/2\pi$ (THz)	$\gamma/2\pi$ (THz)	a(Å^2)	$\omega/2\pi$ (THz)	$\gamma/2\pi$ (THz)	μ(Å^2)
0.97 ± 0.05	0.99	0.0981	0.034	0.99	0.126	0.004
	1.21	0.090	0.038			
1.80 ± 0.05	1.80	0.189	0.092	1.83	0.148	0.007
1.98 ± 0.05	2.03	0.180	0.180	2.03	0.177	0.166
	2.40	0.203	0.677			

part of Fig. 3(c). The obtained parameters including μ_i are also listed in Table I.

IV. ANALYSIS AND DISCUSSION

On the basis of the results presented above, we discuss the terahertz-radiation mechanism in DCMBI. As seen in Figs. 3(a)–3(c) and Table I, the central frequencies of the peak structures observed in the terahertz-radiation spectrum for $E^{\omega}||b$ correspond with those of Raman and infrared-active phonon modes, which is also detailed in the Supplemental Material, S2 [16]. When the spectral width of the incident femtosecond laser pulse (~5 THz) exceeds the frequency of Raman-active phonons, these modes are coherently excited, which is detailed in the Supplemental Material, S3 [16]. This process is called impulsive stimulated Raman scattering (ISRS) [19–21]. If those phonons are also infrared active, they produce oscillations of corresponding polarizations, resulting in narrowband terahertz radiations as discussed in the study of TeO_2 [22]. In the case of the terahertz radiation obtained for $E^{\omega}||c$, it would be related to the phonon modes with k vector parallel to the a axis, which can be detected by using a (011)-surface crystal, which is detailed in the Supplemental Material, S2 [16]. However, the obtained crystal has a (100) surface. Thus, here, we focus on the results obtained for $E^{\omega}||b$.

To demonstrate an ISRS-induced terahertz radiation, we formulate it and evaluate the spectrum of the corresponding $\chi^{(2)}$. The amplitude of the phonon mode is given by $Q(t) = \int_{-\infty}^{t} dt' G_{11}(t-t') \sum_{kl} R_{jk} E_j(t') E_k^*(t')$ [21]. Here, G_{11} is a Green's function and R_{jk} is a Raman tensor. $Q(\omega)$ is expressed by $Q(\omega) = R_{jk} \frac{c^2k^2 - \varepsilon_\infty \omega^2}{\varepsilon_\infty [\omega^4 + \omega^3(2i\gamma) - \omega^2 \frac{c^2k^2 - \varepsilon_\infty \omega_{\mathrm{TO}}^2}{\varepsilon_\infty} - \omega \frac{2i\gamma c^2 k^2}{\varepsilon_\infty} + \frac{\omega_{\mathrm{TO}}^2 c^2 k^2}{\varepsilon_\infty}]} E_j(\omega) E_k^*(\omega)$, as detailed in the Supplemental Material, S3 [16]. Here, γ is a damping constant and ε_∞ is an infinite dielectric constant. By taking into account the conservation law of the wave vector, i.e., $k = 0$, and the Lyddane-Sachs-Teller relation ($\omega_{\mathrm{LO}}^2 = \frac{\varepsilon_0 \omega_{\mathrm{TO}}^2}{\varepsilon_\infty}$), $Q(\omega)$ is given by $Q(\omega) = -\frac{R_{jk}}{\omega^2 - \omega_{\mathrm{LO}}^2 + 2i\gamma\omega} E_j(\omega) E_k^*(\omega)$ [21]. The nonlinear polarization due to ISRS is represented by $P_i(\omega) = N\mu_i Q(\omega) = \varepsilon_0 \chi_{ijk}^{(2)\mathrm{ISRS}} E_j(\omega) E_k^*(\omega)$. Here, we assume that only a single excited state with the energy ω_Δ contributes to the Raman scattering process and an excitation light is in the transparent region (an off-resonant condition). In this case, R_{jk} can be expressed as $R_{jk} = \frac{e^2}{\varepsilon_0 \hbar^2} [\frac{2(\omega_{\mathrm{eg}} - \omega_{\mathrm{Laser}}) a_{jk}}{(\omega_\Delta - \omega_{\mathrm{Laser}})^2 + \omega_i^2}]$, where ω_{eg} is the energy between excited and ground states. Then, we get $\chi_{ijk}^{(2)\mathrm{ISRS}}(\omega_i = \omega_j - \omega_k) = -\frac{Ne^3}{\varepsilon_0^2 \hbar^2} \frac{\mu}{\omega^2 - \omega_{\mathrm{LO}}^2 + 2i\gamma\omega} [\frac{2(\omega_{\mathrm{eg}} - \omega_{\mathrm{Laser}}) a_{jk}}{(\omega_\Delta - \omega_{\mathrm{Laser}})^2 + \omega_i^2}]$. By setting ω_Δ and ω_{Laser} to be the resonant energy (6.7 eV) derived from the Sellmeier relationship [see Fig. 1(d)] and the laser photon energy (1.55 eV), respectively, and using the values of μ, a, γ, and ω_{LO} listed in Table I, we calculate the $|\chi_{cbb}^{(2)\mathrm{ISRS}}|$ spectrum, which is shown by the solid line in Fig. 3(d). $|\chi_{cbb}^{(2)\mathrm{ISRS}}|$ is enhanced with resonance to three Raman- and IR-active phonon modes shown by blue arrows and reaches the maxima of ~0.0035 pm/V. The $|\chi_{cbb}^{(2)\mathrm{ISRS}}|$ spectrum is similar to the terahertz-radiation spectrum shown in Fig. 3(a) (blue circles) except for the broad structure at 1.2–1.7 THz. It is reasonable to consider that this broad structure observed for $E^{\omega}||b$ as well as $E^{\omega}||c$ originates from the OR. By using $|\chi_{cbb}^{(2)\mathrm{ISRS}}|$ and taking the detector response function into account [22], we calculate the electric field $E_X(t)$ of the terahertz radiation for $E^{\omega}||b$ and use it to fit the experimental data, which is shown by the solid line in Fig. 4. The time delay is arbitrary. The calculated curve almost reproduces the experimental data for $E^{\omega}||b$. This result suggests that the terahertz radiation for $E^{\omega}||b$ is dominated mainly by the IR-active phonon mode excited via the ISRS mechanism.

Finally, we discuss the characteristic of ISRS-induced narrowband terahertz radiations in DCMBI, compared to other organic ferroelectrics, in which OR is dominant [6,7]. In the case of croconic acid, the emitted waveform shows the broad spectrum with the frequency component up to 2 THz. This can be explained by OR [6]. In croconic acids, the longitudinal

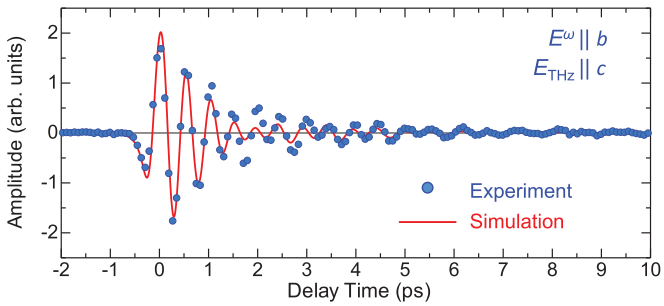

FIG. 4. Terahertz waveform obtained for $E^{\omega}||b$ (circles) and simulation curve originating from the impulsive stimulated Raman scattering (solid line).

direction of all molecules is parallel to the hydrogen-bonding direction, i.e., ferroelectric polarization. Since the asymmetric π-electron configuration is related to the magnitude of $\chi^{(2)}$, this arrangement results in the enhancement of OR. Indeed, $|E_{\mathrm{THz}}(0)|$ in the croconic acid is comparable to that in ZnTe, which is a typical terahertz emitter. On the other hand, in the case of DCMBI, the longitudinal direction of all molecules along the b axis [indicated by the blue shaded area in Fig. 1(a)] is perpendicular to the hydrogen-bonding direction, i.e., ferroelectric c axis, which results in the reduction of OR. This scenario is consistent with the measured light-polarization dependence of the terahertz radiation shown in Figs. 2(b) and 2(c); ISRS is dominant for $E^{\omega}||b$ [Fig. 2(c)], while OR is dominant for $E^{\omega}||c$ [Fig. 2(b)]. In addition, in DCMBI, Raman- and IR-active modes exist in the measured frequency region and thus $E_{\mathrm{THz}}(\omega)$ is resonantly enhanced due to the ISRS mechanism, as revealed by the present work.

V. SUMMARY

In summary, we successfully observed the emission of the narrowband terahertz waves in an above-room-temperature organic ferroelectric DCMBI upon irradiation of a femtosecond laser pulse. We concluded that the narrowband terahertz-radiation mechanism is due to ISRS and evaluated the ISRS-induced second-order nonlinear optical susceptibility spectrum in the terahertz region.

ACKNOWLEDGMENTS

We thank M. Tateno for experimental support in an early stage of this study. This work was partly supported by a Grant-in-Aid by MEXT (Grants No. 25-3372, No. 25247049, No. 25600072, No. 15H03549, No. 16H02301, No. 18H01166, and No. 18H01858). M.S. was supported by the Japan Society for the Promotion of Science (JSPS) through the Program for Leading Graduate Schools (MERIT) and JSPS Research Fellowships for Young Scientists.

APPENDIX A: SECOND-ORDER NONLINEAR OPTICAL EFFECT

Since DCMBI is transparent to the excitation light used in terahertz-radiation experiments (1.55 eV) [see Fig. 1(d)], the observed terahertz radiation can be ascribed to the second-order optical nonlinearity characterized by the second-order nonlinear susceptibility $\chi^{(2)}$. In the transparent media, the polarization $P^{(2)}$ induced by an irradiation with a laser pulse below band gap is represented by

$$P_i^{(2)} = \epsilon_0 \chi_{ijk}^{(2)} E_j^{\omega} E_k^{\omega *}, \tag{A1}$$

where ϵ_0 is the vacuum permittivity and E^{ω} is the light electric field [2]. Since a femtosecond laser pulse has a finite spectral width ~5 THz, the mixing of different frequency components induces the corresponding $P^{(2)}$, resulting in the emission of broadband terahertz waves [8].

The space group of DCMBI is $mm2$ [11]; thus the nonzero components of $\chi^{(2)}$ are χ_{aac}, χ_{aca}, χ_{bbc}, χ_{bcb}, χ_{caa}, χ_{cbb}, and χ_{ccc}, where a, b, and c stand for crystallographic axes [2].

Then, $P^{(2)}$ using the contradicted d tensor is expressed as

$$P^{(2)} = \begin{pmatrix} P_a^{(2)} \\ P_b^{(2)} \\ P_c^{(2)} \end{pmatrix} = \epsilon_0 \begin{pmatrix} 2d_{31} E_a^{\omega} E_c^{\omega *} \\ 2d_{32} E_b^{\omega} E_c^{\omega *} \\ d_{31} E_a^{\omega} E_a^{\omega *} + d_{32} E_b^{\omega} E_b^{\omega *} + d_{33} E_c^{\omega} E_c^{\omega *} \end{pmatrix}. \tag{A2}$$

When the c axis of the crystal with the largest bc surface is set parallel to the X axis (horizontal axis) in laboratory coordinates [Fig. 2(a)], the X-axis electric-field component $E_X(\omega)$ of the terahertz radiation is given by Eq. (1).

To investigate the angle (θ) dependence of the terahertz radiation, we rotate the direction of the electric field (E^{ω}) of the incident femtosecond laser pulse by using a half-wave plate and evaluate the X- and Y-axes components [$E_X(t)$ and $E_Y(t)$] of terahertz electric fields $E_{\mathrm{THz}}(t)$ by means of the vector analysis using two wire-grid polarizers (WG1 and WG2), as schematically shown in Fig. 2(a). With respect to

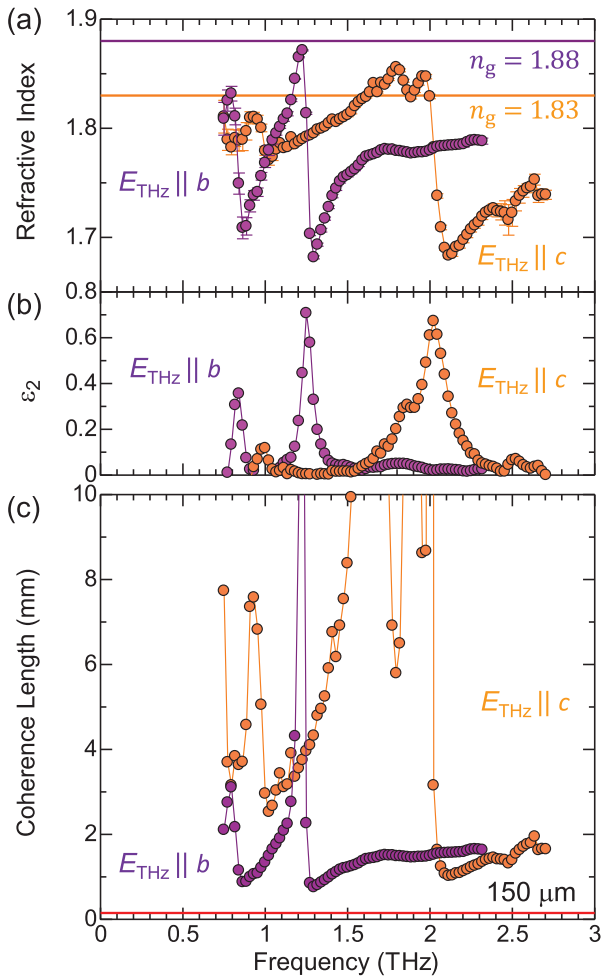

FIG. 5. Spectra of (a) refractive index and (b) imaginary part of the dielectric constant ε_2 along the b and c axes. (b) Calculated coherence length along the b and c axes, which exceeds the sample thickness [150 μm indicated by the horizontal red (gray) line] used in the terahertz-radiation experiments.

TABLE II. Selection rule of Raman-active modes and mode assignments using *bc*-, *ab*-, and *ac*-surface crystals in the backscattering geometry. Asterisk indicates the mode due to the leakage.

Configurations	Representations	$A_1(z)$ TO (THz)	$A_1(z)$ LO (THz)	A_2 (THz)	$B_1(x)$ (THz)	$B_2(y)$(THz)
$b(aa)\overline{b}$	$A_1(z)$ TO	0.99 2.40	1.20* 2.05*			
$b(cc)\overline{b}$	$A_1(z)$ TO	0.99 2.40			0.82*	
$b(ac)\overline{b}$	$B_1(x)$				0.82 1.3 2.4 2.67	
$b(ca)\overline{b}$	$B_1(x)$				0.82 1.3 2.4 2.67	
$c(bb)\overline{c}$	$A_1(z)$ LO		0.99 1.21 1.80 2.06 2.38		0.82*	
$c(aa)\overline{c}$	$A_1(z)$ LO		0.99 1.21 1.80 2.06 2.38			
$c(ab)\overline{c}$	A_1		1.20*	0.82 1.77 2.40		
$c(ba)\overline{c}$	A_1		1.20*	0.82 1.77 2.40		
$a(cc)\overline{a}$	$A_1(z)$ TO	0.99 2.40		1.70*		
$a(bb)\overline{a}$	$A_1(z)$ TO	0.98 2.40	1.20* 2.05*			
$a(cb)\overline{a}$	$B_2(y)$					1.80 2.30 2.67
$a(bc)\overline{a}$	$B_2(y)$					1.80 2.30 2.67

the X axis, the angle of WG2 is set at 0°, while that of WG1 is set at +45° or −45°. We measure the corresponding electric fields, $E_{+45^\circ}(t)$ and $E_{-45^\circ}(t)$, and obtain $E_X(t)$ and $E_Y(t)$ from the relations, $E_X(t) = \frac{1}{\sqrt{2}}[E_{+45^\circ}(t) - E_{-45^\circ}(t)]$ and $E_Y(t) = \frac{1}{\sqrt{2}}[E_{+45^\circ}(t) + E_{-45^\circ}(t)]$, respectively. Further information concerning the calculation procedure of $E_X(t)$ and $E_Y(t)$ by the vector analysis is reported in Refs. [6,14,15].

APPENDIX B: ESTIMATION OF COHERENCE LENGTH

In order to estimate the coherence length (l_c) for terahertz radiation, we measured the polarized transmission spectra in the terahertz region by terahertz time-domain spectroscopy and estimated the complex optical constants. Our estimation procedure is reported in Ref. [22]. In this experiment, we used a 397-μm-thick crystal with the largest *bc* surface. Figure 5(a) shows the spectra of the refractive index n_{THz} along the *c* and *b* axes, which are shown by orange and purple circles, respectively. In both configurations, the clear dispersion structures are discerned. Accordingly, the peak structures appear in spectra of the imaginary part of the dielectric constant ε_2 at 0.99, 1.84, and 2.02 THz for the *c* axis, and at 0.86, 1.25, and 1.8 THz for the *b* axis, which are shown by orange and purple circles, respectively, in Fig. 5(b). We also indicate the value of the group refractive index n_g at 1.55 eV by horizontal lines in Fig. 5(a)—1.88 ($E^\omega||b$) and 1.83 ($E^\omega||c$), which are obtained by the Sellmeier relation from the refractive index spectra shown in Fig. 1(c).

l_c is represented by $\frac{\lambda}{2}\frac{1}{|n_g - n_{THz}|}$, where λ is the wavelength of the emitted terahertz waves. We estimated the spectra of l_c along the c and b axes, which are shown by orange and purple circles in Fig. 5(c), respectively. In both configurations, the increase of l_c in the narrow-frequency region occurs by satisfying the phase-matching condition ($n_g \sim n_{THz}$) due to the presence of the sharp dispersion of the phonon modes in the terahertz region, as seen in Fig. 5(a). This would produce the narrowband terahertz radiation, which is indeed observed near the phonon-polariton resonance in ZnTe [23] and the F_2 mode in $Bi_4Ge_3O_{12}$ [17]. In our terahertz-radiation experiments for $E^\omega||c$ and $E^\omega||b$, we detected the power spectra of the terahertz radiations polarized along the c axis. Thus, the observed terahertz radiation may be related to the increase of l_c along the c axis; i.e., the peak structures in the spectrum of l_c may appear in the power spectra of terahertz radiations. However, this possibility is clearly excluded. The sample thickness used in terahertz-radiation experiments was set to be 150 μm [horizontal red line in Fig. 5(c)]. This value is shorter than the minimum value of l_c, i.e., 1 mm at 2.1 THz. Thus, in our experimental condition, the good phase-matching condition is satisfied in the measured frequency region (0–3 THz). In addition, the observed anisotropic power spectra of terahertz radiation obtained for $E^\omega||c$ and $E^\omega||b$ [Fig. 3(a)] cannot be reproduced by the spectrum of l_c along the c axis. These results clearly rule out the possibility of the phase-matching-induced narrowband terahertz radiation in DCMBI.

APPENDIX C: POLARIZED RAMAN SPECTRA IN THE TERAHERTZ REGION

Raman tensors of DCMBI with the point group of $mm2$ are given by

$$A_1(z) = \begin{pmatrix} a & 0 & 0 \\ 0 & b & 0 \\ 0 & 0 & c \end{pmatrix}, \quad A_2 = \begin{pmatrix} 0 & d & 0 \\ d & 0 & 0 \\ 0 & 0 & 0 \end{pmatrix},$$

$$B_1(x) = \begin{pmatrix} 0 & 0 & e \\ 0 & 0 & 0 \\ e & 0 & 0 \end{pmatrix}, \quad B_2(y) = \begin{pmatrix} 0 & 0 & 0 \\ 0 & 0 & f \\ 0 & f & 0 \end{pmatrix}, \quad \text{(C1)}$$

where a, b, c, d, e, and f are constant. We listed in Table II the Raman selection rule given by Eq. (C1). In order to assign the Raman modes of DCMBI in the terahertz region, we measured the polarized Raman spectra using bc-, ab-, and ac-surface crystals in the backscattering geometry, the results of which in the frequency region of 0.5–3.5 THz are summarized in Figs. 6(a)–6(c), respectively. According to the Raman selection rule listed in Table II, the $B_1(x)$ mode is active for the $b(ac)\bar{b}$ and $b(ca)\bar{b}$ configurations. The obtained Raman spectra in $b(ac)\bar{b}$ and $b(ca)\bar{b}$ configurations are shown by pink and black lines in Fig. 6(c), respectively. There are peak structures at 0.82, 1.3, 2.4, and 2.67 THz in both spectra, which are all assigned to this mode. On the other hand, the $B_2(y)$ mode is active for the $a(bc)\bar{a}$ and $a(cb)\bar{a}$ configurations, the results of which are shown by orange and yellow lines in Fig. 6(a), respectively. We observe the peak structures at 0.82, 1.3, 2.3, and 2.67 THz in both spectra and assigned them to this mode. In Raman spectra obtained for $c(ab)\bar{c}$ and $c(ba)\bar{c}$ configurations, which are shown by sky blue and brown lines in Fig. 6(b),

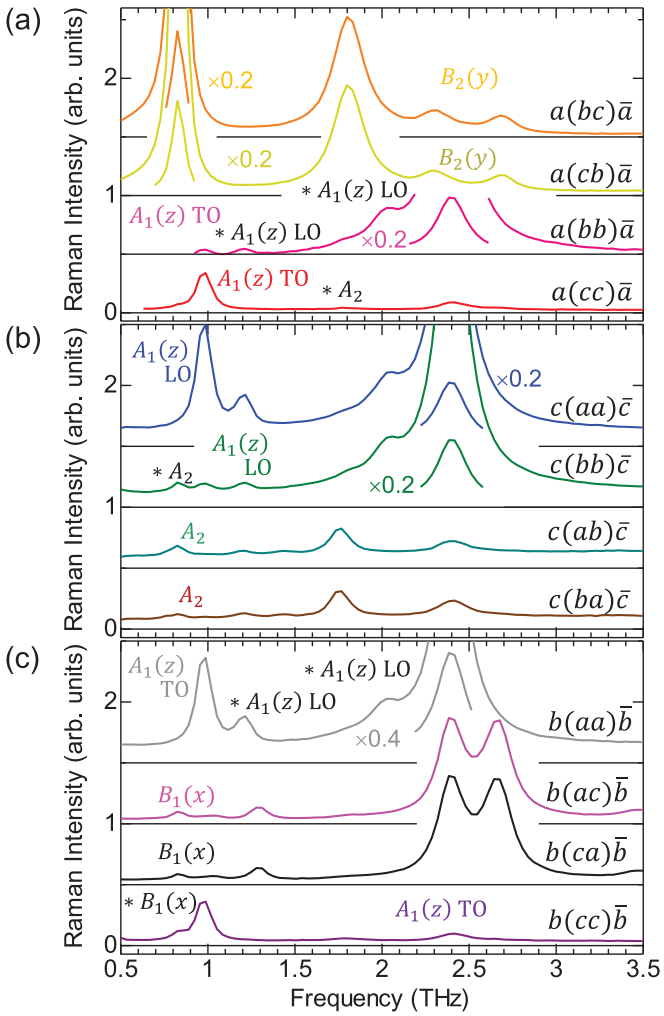

FIG. 6. Polarized Raman scattering spectra in the terahertz region obtained using (a) bc-, (b) ab-, and (c) ac-surface crystals in the backscattering geometry.

only the A_2 mode appears. A_2 modes can be discerned at 0.82, 1.2, 1.77, and 2.4 THz. The $A_1(z)$ transverse-optical (TO) phonon mode becomes active for $a(bb)\bar{a}$, $a(cc)\bar{a}$, $b(aa)\bar{b}$, and $b(cc)\bar{b}$ configurations. As seen in the Raman spectrum in the $a(bb)\bar{a}$ configuration, which is shown by a red line in Fig. 6(a), we observe two clear peak structures at 0.99 and 2.4 THz and a tiny peak structure at 1.77 THz indicated by an asterisk. The former two peak structures are also discerned in the Raman spectrum in the $b(cc)\bar{b}$ configuration, which is shown by a purple line in Fig. 6(c). Thus, the peak structures at 0.99 and 2.4 THz are assigned to the $A_1(z)$ TO phonon modes. The peak structure (1.77 THz) is due to the leakage of the A_2 mode, which is seen in the Raman spectra in the $c(ab)\bar{c}$ and $c(ba)\bar{c}$ configurations [Fig. 6(b)]. In the Raman spectrum in the $b(cc)\bar{b}$ configuration [Fig. 6(c)], there is a tiny peak structure at 0.82 THz, which is assigned to the leakage of the B_1 mode, as discerned in the Raman spectra in the $b(ac)\bar{b}$ and $b(ca)\bar{b}$ configurations. On the other hand, the $A_1(z)$ longitudinal-optical (LO) phonon mode becomes active for the $c(aa)\bar{c}$ and $c(bb)\bar{c}$ configurations, the obtained Raman spectra of which are shown by blue and green lines in Fig. 6(b), respectively. In both configurations, peak structures

show up at 0.99, 1.21, 1.80, 2.06, and 2.38 THz, which are assigned to the $A_1(z)$ LO modes. A tiny peak structure at 0.82 THz obtained for the $c(bb)\bar{c}$ configuration is the leakage of the A_1 mode, which is indicated by an asterisk. In the $a(bb)\bar{a}$ and $b(aa)\bar{b}$ configurations, where the $A_2(z)$ TO mode is active, tiny peak structures at 1.2 and 2.0 THz indicated by asterisks are observed as shown by a pink line in Fig. 6(a) and by a gray line in Fig. 6(c), respectively. These structures are due to leakages of $A_1(z)$ LO modes. We listed in Table II results of the Raman mode assignments.

[1] M. E. Lines and A. M. Glass, *Principles and Applications of Ferroelectric and Related Materials* (Clarendon, Oxford, 1977).

[2] Y. R. Shen, *The Principles of Nonlinear Optics* (Wiley, New York, 1984).

[3] S. Horiuchi and Y. Tokura, Organic ferroelectrics, Nat. Mater. **7**, 357 (2008).

[4] S. Horiuchi, Y. Tokunaga, G. Giovannetti, S. Picozzi, H. Itoh, R. Shimano, R. Kumai, and Y. Tokura, Above-room-temperature ferroelectricity in a single-component molecular crystal, Nature (London, U. K.) **463**, 789 (2010).

[5] S. Horiuchi, R. Kumai, and Y. Tokura, Hydrogen-bonding molecular chains for high-temperature ferroelectricity, Adv. Mater. **23**, 2098 (2011).

[6] M. Sotome, N. Kida, S. Horiuchi, and H. Okamoto, Visualization of ferroelectric domains in a hydrogen-bonded molecular crystal using emission of terahertz radiation, Appl. Phys. Lett. **105**, 041101 (2014).

[7] W. Guan, N. Kida, M. Sotome, Y. Kinoshita, R. Takeda, A. Inoue, S. Horiuchi, and H. Okamoto, Terahertz radiation by optical rectification in a hydrogen-bonded organic molecular ferroelectric crystal, 2-phenylmalondialdehyde, Jpn. J. Appl. Phys. **53**, 09PD07 (2014).

[8] M. Bass, P. A. Franken, J. F. Ward, and G. Weinreich, Optical Rectification, Phys. Rev. Lett. **9**, 446 (1962).

[9] M. Tonouchi, Cutting-edge terahertz technology, Nat. Photonics **1**, 97 (2007).

[10] A. Schneider, M. Neis, M. Stillhart, B. Ruiz, R. U. A. Khan, and P. Günter, Generation of terahertz pulses through optical rectification in organic DAST crystals: Theory and experiment, J. Opt. Soc. Am. B **23**, 1822 (2006).

[11] S. Horiuchi, F. Kagawa, K. Hatahara, K. Kobayashi, R. Kumai, Y. Murakami, and Y. Tokura, Above-room-temperature ferroelectricity and antiferroelectricity in benzimidazoles, Nat. Commun. **3**, 1308 (2012).

[12] M. Sotome, N. Kida, S. Horiuchi, and H. Okamoto, Terahertz radiation imaging of ferroelectric domain topography in room-temperature hydrogen-bonded supramolecular ferroelectrics, ACS Photonics **2**, 1373 (2015).

[13] M. Sotome, N. Kida, Y. Kinoshita, H. Yamakawa, T. Miyamoto, H. Mori, and H. Okamoto, Visualization of a nonlinear conducting path in an organic molecular ferroelectric by using emission of terahertz radiation, Phys. Rev. B **95**, 241102(R) (2017).

[14] Y. Kinoshita, N. Kida, M. Sotome, R. Takeda, N. Abe, M. Saito, T. Arima, and H. Okamoto, Visualization of ferroelectric domains in boracite using emission of terahertz radiation, Jpn. J. Appl. Phys. **53**, 09PD08 (2014).

[15] Y. Kinoshita, N. Kida, M. Sotome, T. Miyamoto, Y. Iguchi, Y. Onose, and H. Okamoto, Terahertz radiation by subpicosecond magnetization modulation in the ferrimagnet $LiFe_5O_8$, ACS Photonics **3**, 1170 (2016).

[16] See Supplemental Material at http://link.aps.org/supplemental/10.1103/PhysRevA.98.013843 for ferroelectric domain structure visualized by terahertz-radiation imaging, comparison terahertz-emission spectra with Raman and dielectric constant spectra, and impulsive stimulated Raman scattering process.

[17] R. Takeda, N. Kida, M. Sotome, Y. Matsui, and H. Okamoto, Circularly polarized terahertz radiation from a eulytite oxide by a pair of femtosecond laser pulses, Phys. Rev. A **89**, 033832 (2014).

[18] M. Grimsditch and M. Cardona, Absolute cross-section for Raman scattering by phonons in silicon, Phys. Status Solidi B **102**, 155 (1980).

[19] Y.-X. Yan and K. A. Nelson, Impulsive stimulated light scattering. I. General theory, J. Chem. Phys. **87**, 6240 (1987).

[20] Y.-X. Yan and K. A. Nelson, Impulsive stimulated light scattering. II. Comparison to frequency-domain light-scattering spectroscopy, J. Chem. Phys. **87**, 6257 (1987).

[21] T. P. Dougherty, G. P. Wiederrecht, and K. A. Nelson, Impulsive stimulated Raman scattering experiments in the polariton regime, J. Opt. Soc. Am. B **9**, 2179 (1992).

[22] M. Sotome, N. Kida, R. Takeda, and H. Okamoto, Terahertz radiation induced by coherent phonon generation via impulsive stimulated Raman scattering in paratellurite, Phys. Rev. A **90**, 033842 (2014).

[23] C. M. Tu, S. A. Ku, W. C. Chu, C. W. Luo, J. C. Chen, and C. C. Chi, Pulsed terahertz radiation due to coherent phonon-polariton excitation in⟨110⟩ZnTe crystal, J. Appl. Phys. **112**, 093110 (2012).